Small Signal Model for Very-Large-Scale Multi-Active-Bridge Differential Power Processing (MAB-DPP) Architecture

Ping Wang, Yenan Chen, Youssef Elasser, Minjie Chen
Princeton University, Princeton, NJ, United States
Email: {pwang2, yenanc, yelasser, minjie}@princeton.edu

***Abstract*—Differential power processing (DPP) is applicable to a wide range of applications. This paper systematically investigates the small signal model of very-large-scale multi-active-bridge differential power processing (MAB-DPP) architecture. The proposed small signal model captures the impact of power losses and provides an accurate and comprehensive understanding about the dynamics of the MAB-DPP converter. The model is compact and highly scalable to very-large-scale MAB-DPP systems. The phase-to-voltage transfer function of a MAB-DPP architecture with an arbitrary number of ports was derived and validated by both SPICE simulations and experimental results. This paper also developed a distributed voltage control strategy, namely distributed phase-shift (DPS) control, which offers high scalability with low computational cost. A 10-port MAB-DPP prototype which can support hot-swapping with a significant step load transient was built and tested to verify the effectiveness of the proposed small signal model and the control strategy.**

***Index Terms*—multi-active-bridge, differential power processing, series-stacked architecture, small signal model, distributed control, very-large-scale power electronics systems**

I. Introduction

Many emerging energy systems, such as solar farms, grid-scale energy storage and large-scale data centers, comprise hundreds or thousands of modular units connected in series or parallel as a sophisticated network. For batteries, solar cells, and computer servers, differential power processing (DPP) can minimize the power conversion stress and can greatly improve the performance of series-stacked energy systems [1], [2].

One way to implement a DPP architecture is to connect each series-connected voltage domain to a dc voltage bus through an isolated dc-dc converter (dc-coupled DPP architecture [2], [3]). This implementation requires high component count, multiple magnetic components, and many redundant "dc-ac-dc" power conversion stages. By coupling many series-stacked voltage domain with a single multi-winding transformer through an array of "dc-ac" units (Fig. 1), the "ac-coupled" DPP architecture can reduce the power conversion stress and the component count, and can significantly improve the system efficiency [4]. Ac-coupled DPP architectures can also offer high scalability and high power density, and are very promising options towards very-large-scale differential power processing systems.

One way to implement an ac-coupled DPP architecture is to design each dc-ac unit as an active bridge as shown in Fig. 2. The converter operates as a multi-active-bridge converter with

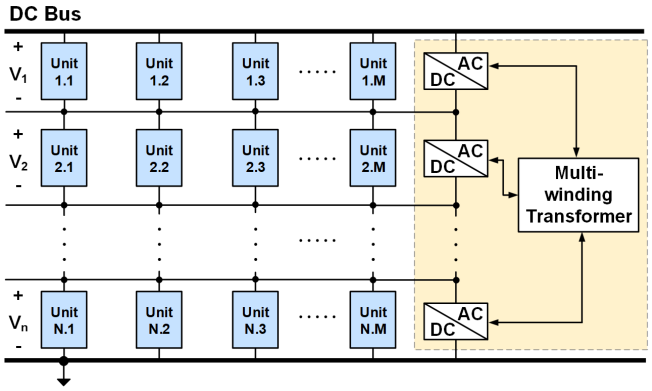

Fig. 1. Ac-coupled DPP architecture for large scale modular dc energy systems. The series-stacked voltage domains can support PV panels, battery cells or computer servers.

all ports connected in series and processes differential power among all ports. Since the maximum magnetic flux density is determined by the maximum voltage-second-per-turn of the windings instead of the winding count, the magnetic core area stays roughly the same as the number of windings increases. This multi-active-bridge differential power processing (MAB-DPP) topology is one of the simplest and most scalable way of implementing an ac-coupled DPP architecture.

One major challenge of designing a MAB-DPP converter with a large number of ports (e.g., more than 100 ports) is to model the sophisticated power flow and the cross-coupled dynamic behaviors. Existing small signal models for the MAB converter and its derivatives only consider the small perturbation of the phase-shift at each port [5], [6]. The impacts of the load structure, port voltage variation and the power conversion losses are neglected. Various small-signal models has been developed to capture the power conversion losses in dual-active-bridge [7]–[9]. These models either applied full-order state-space average model or were derived based on the time-domain inductor current waveforms, making them highly sophisticated and very heavy in computation. It is almost impossible and impractical to extend these models to very-large-scale MAB designs with a large number of ports.

This paper presents a compact and scalable small signal model for the MAB-DPP architecture with an arbitrary number of ports. Each port of the MAB converter is modeled as phase-controlled and voltage-controlled current sources and the power conversion loss is modeled as an output resistance. The impact of the load power and phase-shift of each port

978-1-7281-1842-0/19/$31.00 ©2019 IEEE

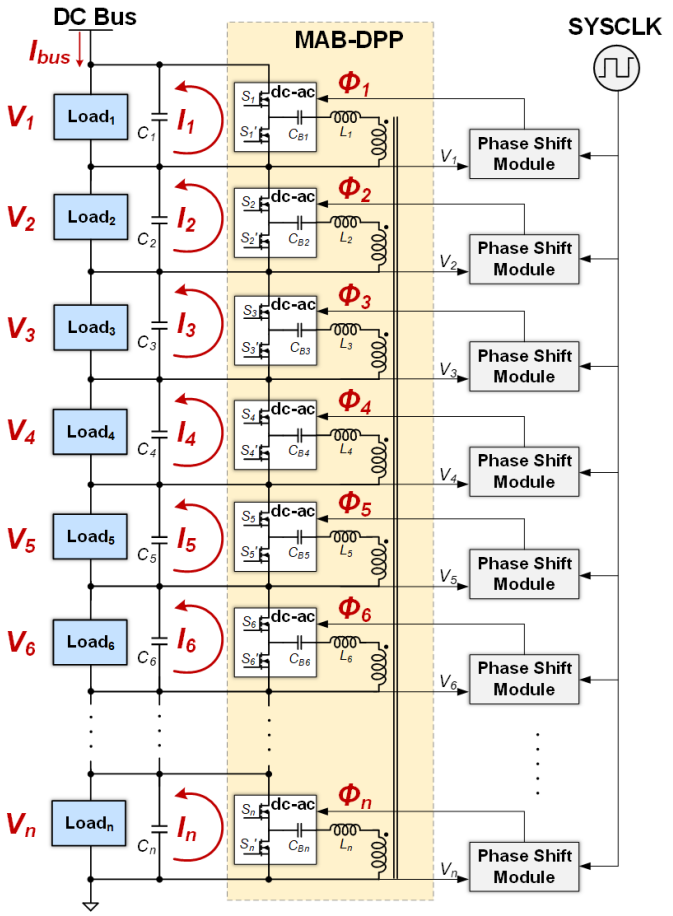

Fig. 2. Block diagram of a MAB-DPP architecture with a large number of ac-coupled voltage domains connected in series.

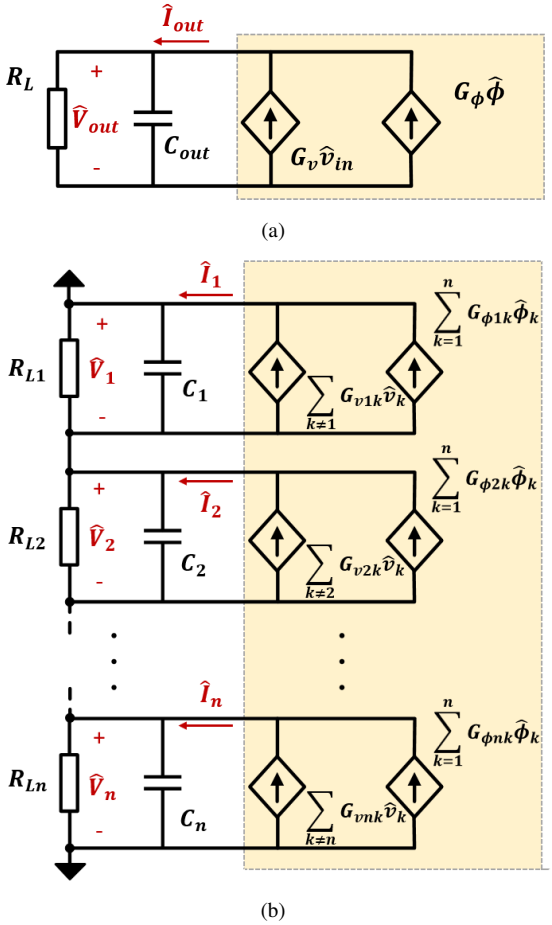

Fig. 3. Small signal model of (a) a DAB converter; (b) a MAB converter.

on the system dynamic response was theoretically analyzed and experimentally verified. Based on the small signal model, a low-cost highly scalable distributed control strategy was proposed and implemented to control a 10-port MAB-DPP prototype. The prototype can support significant load step transients and can achieve extremely high efficiency and power density.

The remainder of this paper is organized as follows: Section II derives the small-signal model of a lossless MAB-DPP architecture. Section III extends the small-signal model to capture the power conversion loss in the MAB-DPP converter. Section IV verifies the small signal model with SPICE simulations. Section V presents a distributed control strategy for the MAB-DPP architecture. The small signal model and the control strategy were experimentally verified in Section VI. Finally, Section VII concludes this paper.

II. Small Signal Model of the MAB-DPP Architecture without Power Loss

Fig. 2 shows the topology of a MAB-DPP architecture. The power flow among multiple ports are closely coupled. The series-stacked connection of the voltage domains maintains constant dc bus voltage and forces each load to share the same bus current. To design and control a MAB-DPP systems with very large number of series-stacked voltage domains, a precise small-signal model which reveals the transfer function from the phase of an arbitrary port (Φ_i) to the voltage of an arbitrary port (V_j) is needed. The average output current of a dual active bridge (DAB) converter implemented with half bridges is [10]:

$$I_{out} = \frac{P_{out}}{V_{out}} = \frac{V_{in}}{4\pi f L_{eq}} \Phi \left(1 - \frac{|\Phi|}{\pi}\right), \tag{1}$$

where L_{eq} is the inductance linking the two ports, Φ is the phase difference between the two ports, and f is the switching frequency. The small signal output current is:

$$\hat{i}_{out} = G_v \hat{v}_{in} + G_\phi \hat{\phi}, \tag{2}$$

$$\begin{cases} G_v = \dfrac{\Phi}{4\pi f L_{eq}} \left(1 - \dfrac{|\Phi|}{\pi}\right) \\ G_\phi = \dfrac{V_{in}}{4\pi f L_{eq}} \left(1 - \dfrac{2|\Phi|}{\pi}\right) \end{cases} \tag{3}$$

As illustrated in Fig. 3a, the small signal model of a DAB converter contains two current sources ($G_v\hat{v}_{in}$ and $G_\phi\hat{\phi}$) depending on $\hat{v}_{in}$ and $\hat{\phi}$. Note $\hat{i}_{out}$ is not a function of $\hat{v}_{out}$ in an ideal lossless DAB.

For a MAB converter, the average output current of port $\#i$ can be derived based on the power flow analysis [4], [11]:

$$I_i = \sum_{j=1}^{n} \frac{V_j}{4\pi f L_{ij}} \Phi_{ij} \left(\frac{|\Phi_{ij}|}{\pi} - 1 \right), \tag{4}$$

where L_{ij} is the equivalent inductance linking port $\#i$ and port $\#j$, and Φ_{ij} is the phase difference between port $\#i$ and port $\#j$. Based on (4), the small-signal current at one port is a function of the voltage perturbation of all ports $\{\hat{v}_1, \hat{v}_2, ..., \hat{v}_n\}$, and phase perturbation of all ports $\{\hat{\phi}_1, \hat{\phi}_2, ..., \hat{\phi}_n\}$:

$$\hat{i}_i = \sum_{j=i}^{n} G_v(i,j)\hat{v}_j + \sum_{j=1}^{n} G_\phi(i,j)\hat{\phi}_j. \tag{5}$$

Here $G_v(i,j)$ and $G_\phi(i,j)$ are functions of the large-signal voltage $\{V_1, V_2, ..., V_n\}$, and the large-signal phase Φ_{ij}:

$$G_v(i,j) = \frac{\Phi_{ij}}{4\pi f L_{ij}} \left(\frac{|\Phi_{ij}|}{\pi} - 1 \right) \tag{6}$$

$$G_\phi(i,j) = \begin{cases} \dfrac{V_j}{4\pi f L_{ij}} \left(1 - \dfrac{2|\Phi_{ij}|}{\pi} \right) & j \neq i, \\ \displaystyle\sum_{k \neq i} \dfrac{V_k}{4\pi f L_{ik}} \left(\dfrac{2|\Phi_{ik}|}{\pi} - 1 \right) & j = i. \end{cases} \tag{7}$$

As shown in Fig. 3b, the small signal output current at each port in MAB can be represented as two current sources determined by the voltage perturbation and the phase perturbation of all ports. Similar to a DAB, the small signal current $\hat{i}_i$ of port $\#i$ is not a function of the voltage perturbation of the same port $\hat{v}_i$, because $G_v(i,i)$ is zero. The output ports of a MAB-DPP architecture are connected to a series stacked $R-C$ network. The series-stacked load structure adds another constraint on the small signal output voltages $\{\hat{v}_1, \hat{v}_2, ..., \hat{v}_n\}$ and output currents $\{\hat{i}_1, \hat{i}_2, ..., \hat{i}_n\}$, which can be described by an impedance matrix:

$$\begin{bmatrix} \hat{v}_1 \\ \hat{v}_2 \\ \vdots \\ \hat{v}_n \end{bmatrix} = \begin{bmatrix} Z_1 || \sum_{k\neq 1} Z_k & -\frac{Z_1 Z_2}{\sum_{k=1}^{n} Z_k} & \cdots & -\frac{Z_1 Z_n}{\sum_{k=1}^{n} Z_k} \\ -\frac{Z_2 Z_1}{\sum_{k=1}^{n} Z_k} & Z_2 || \sum_{k\neq 2} Z_k & \cdots & -\frac{Z_2 Z_n}{\sum_{k=1}^{n} Z_k} \\ \vdots & \vdots & \ddots & \vdots \\ -\frac{Z_n Z_1}{\sum_{k=1}^{n} Z_k} & -\frac{Z_n Z_2}{\sum_{k=1}^{n} Z_k} & \cdots & Z_n || \sum_{k\neq n} Z_k \end{bmatrix} \begin{bmatrix} \hat{i}_1 \\ \hat{i}_2 \\ \vdots \\ \hat{i}_n \end{bmatrix} \tag{8}$$

where Z_i is the lumped load impedance at port i:

$$Z_i = R_{Li} || \frac{1}{sC_i} = \frac{R_{Li}}{sR_{Li}C_i + 1}. \tag{9}$$

Eq. (5) and Eq. (8) can be reorganized as:

$$\begin{cases} \hat{\boldsymbol{i}} = \boldsymbol{G_v} \times \hat{\boldsymbol{v}} + \boldsymbol{G_\phi} \times \hat{\boldsymbol{\phi}}, \\ \hat{\boldsymbol{v}} = \boldsymbol{G_z} \times \hat{\boldsymbol{i}}. \end{cases} \tag{10}$$

Based on Eq (10), the transfer function matrix from the phase perturbation ($\hat{\boldsymbol{\phi}}$) to the port voltage perturbation ($\hat{\boldsymbol{v}}$) in a lossless MAB-DPP architecture is:

$$\hat{\boldsymbol{v}} = (\boldsymbol{I} - \boldsymbol{G_Z G_v})^{-1} \boldsymbol{G_Z G_\phi} \times \hat{\boldsymbol{\phi}} = \boldsymbol{G_S} \times \hat{\boldsymbol{\phi}}. \tag{11}$$

The $n \times n$ transfer function matrix $\boldsymbol{G_S}$ can be used to analyze the stability of the MAB-DPP system and assist in the controller design.

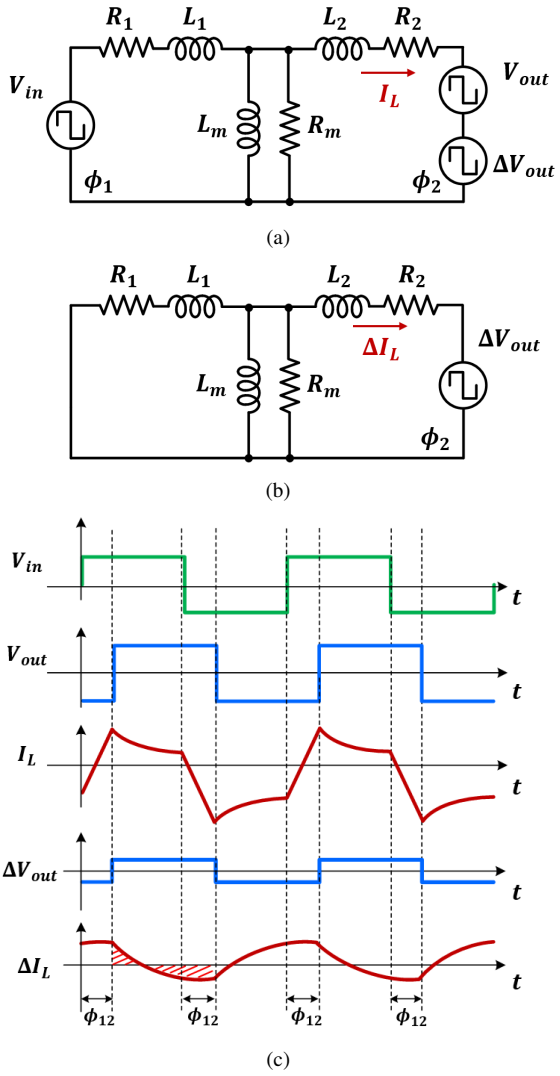

Fig. 4. (a) Equivalent lumped circuit model to analysis the transfer function of a DAB converter. (b) Inductor current variation ΔI_L due to ΔV_{out}. (c) Current and voltage waveforms of DAB with power losses.

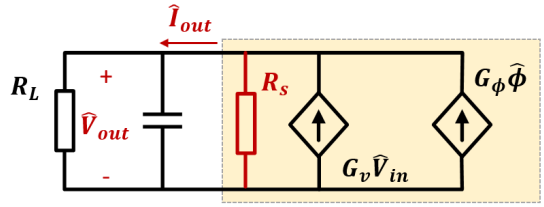

Fig. 5. Improved small signal model of DAB considering power losses.

III. Small Signal Model of the MAB-DPP Architecture Considering Loss

The loss of a MAB converter will change the power flow and reduce the dc gain of the system transfer function. To capture the influence of loss, an improved small signal model was developed. Fig. 4a shows an equivalent circuit of a DAB with the power conversion loss modeled as a few resistors R_1,

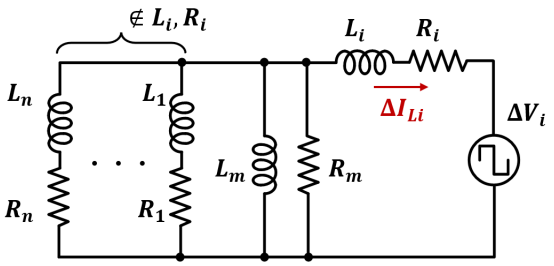

Fig. 6. Equivalent circuit of MAB showing the i^{th} port inductor current variation ΔI_{Li} due to ΔV_i.

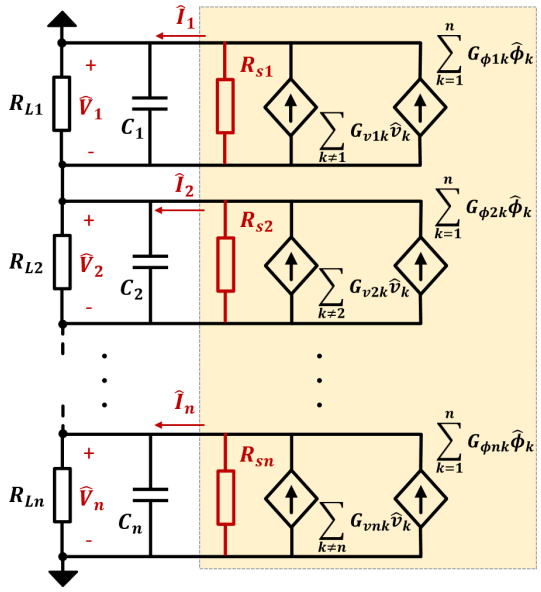

Fig. 7. Improved small signal model of MAB considering power losses

R_2 and R_m. R_1 and R_2 capture the resistance of the inductors, switches and the transformer windings, and R_m captures the core loss. Switching losses can be included in either R_1, R_2, or R_m. With significant R_1, R_2, and R_m, Eq. (1) is no longer valid and needs to be modified. As illustrated in Fig. 4c, the inductor current is no longer trapezoidal but has a significant exponential component. The lower the quality factor of the equivalent $L-R$ circuit, the more different the inductor current was from the trapezoidal waveform. $G_v(i,j)$ and $G_\phi(i,j)$ need to be modified to capture the impact of these resistors. One of the most distinct difference is in $G_v(i,i)$. As previously described, the output current perturbation ($\hat{i}_i$) of an ideal MAB converter has no correlation with the voltage perturbation ($\hat{v}_i$) at the same port (i.e. $G_v(i,i)=0$). However, this observation is not valid if losses are considered. As shown in Fig. 4, assuming that there is a voltage perturbation (ΔV_{out}) on the output voltage, the change of the inductor current (ΔI_L) can be considered as if there is only one square wave voltage source (ΔV_{out}), based on superposition. The change on the average output current (ΔI_{out}) is the time average integral of ΔI_L in the positive half cycle of ΔV_{out}, which is not zero if the current waveform is exponential. As a result, one additional current source, $G_{vout}\hat{v}_{out}$, should be added to the small signal model of Fig. 3a, which can be modeled as an output resistance $R_s = -1/G_{vout}$ (Fig. 5) to capture this effect. Fig. 4b indicates that the ΔI_{out} is only determined by ΔV_{out} and is not related with the phase-shift operating point (Φ_{12}). If the impedances of R_m and L_m are much larger than R_1, R_2, L_1 and L_2, the effective output resistance of a DAB converter can be derived analytically as:

$$R_s = -\frac{1}{G_{vout}} = \frac{(R_1+R_2)}{\frac{1}{4} - \frac{\tau\left(1-\exp\left(-\frac{T}{2\tau}\right)\right)}{T\left(1+\exp\left(-\frac{T}{2\tau}\right)\right)}}, \qquad (12)$$

in which the time constant $\tau = (L_1+L_2)/(R_1+R_2)$.

In a MAB architecture, the output current perturbation caused by the voltage perturbation at the same port can be interpreted as a square wave voltage source (ΔV_i) driving a linear $L-R$ network, as shown in Fig. 6. Also, the induced output current change ΔI_i is only determined by the ΔV_i, and is not related with the phase-shift $\{\Phi_1, \Phi_2, ..., \Phi_n\}$. The corresponding current source $G_v(i,i)\hat{v}_i$ can be interpreted as an output resistance R_{si} added at each port, as shown in Fig. 7. For a MAB-DPP architecture, Eq. (9) should be modified if losses are considered:

$$Z_i = R_{Li}||R_{si}||\frac{1}{sC_i} = \frac{(R_{Li}||R_{si})}{s(R_{Li}||R_{si})C_i+1}. \qquad (13)$$

With the modified impedance matrix, the improved system transfer function can be derived from Eq. (11). The output resistance of each port R_{si} can be estimated by circuit analysis, SPICE simulations, or experimental calibriation (by measuring $\Delta I_i/\Delta V_i$ while keeping all the phase-shifts and voltages of all other ports constant). Once R_{si} is found, the small signal model and the transfer function can be modified accordingly.

TABLE I
SIMULATION PARAMETERS

Parameter		Value
Switching Frequency (f_{sw})		100 kHz
External Inductance ($L_1 \sim L_{10}$)		120 nH
Magnetic Inductance (L_m)		3.2 μH
Output Capacitance ($C_1 \sim C_{10}$)		200 μF
Equivalent Path Resistance ($R_1 \sim R_{10}$)		20 mΩ
Magnetic Resistance (R_m)		220 Ω
Load Resistance	$R_{L1} \sim R_{L9}$	10 Ω
	R_{L10}	3 Ω

IV. SPICE Simulation Verification

A. 10-Port MAB-DPP Converter with and without Losses

To validate the effectiveness of the proposed small signal model, a 10-port MAB-DPP converter which connects ten 5 V voltage domains in series was simulated in SPICE. The circuit parameters are listed in the Table I. The MAB-DPP converter can deliver power from n arbitrary ports to m arbitrary ports with high efficiency and high power density. In this example analysis, we investigate the transfer function matrix with the MAB-DPP converter delivering power from nine ports (port

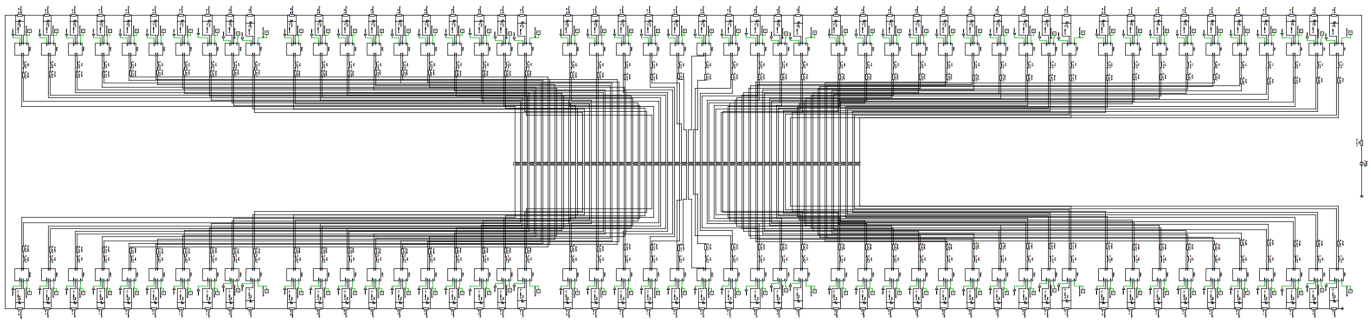

Fig. 8. SPICE simulation platform of a 100-port lossless MAB-DPP converter in PLECS.

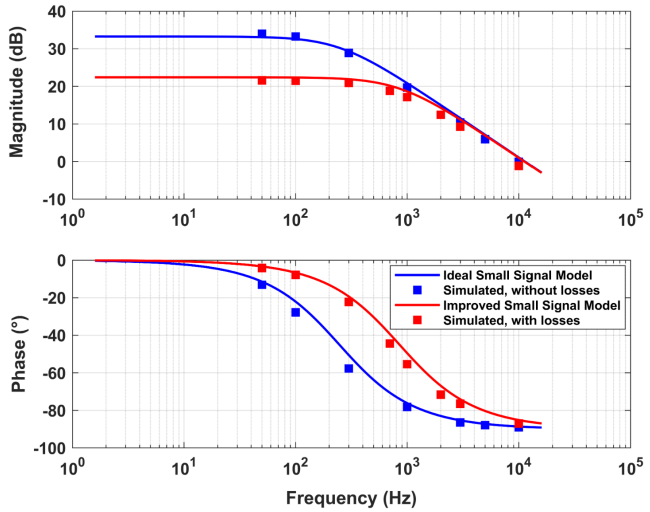

Fig. 9. Comparison between calculated and simulated transfer function of a 10-port MAB-DPP converter with and without power losses.

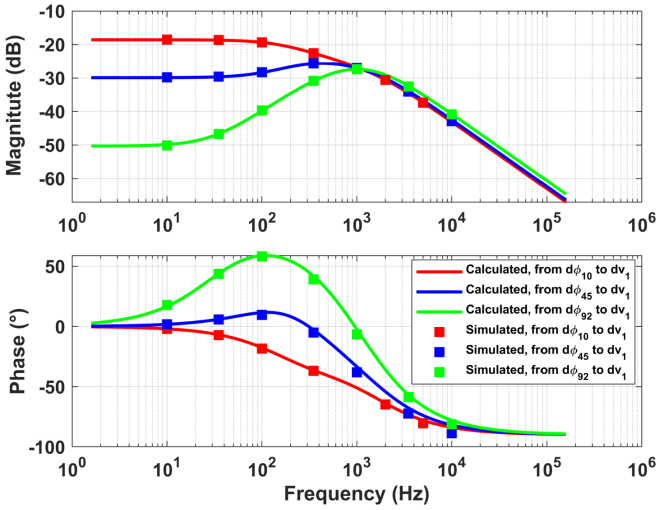

Fig. 10. Calculated and simulated v to ϕ bode plots for three arbitrary ports in a 100-port MAC-DPP system: (1) transfer function from $\hat{\phi}_{10}$ to $\hat{v}_1$; (2) from $\hat{\phi}_{45}$ to $\hat{v}_1$; (3) from $\hat{\phi}_{92}$ to $\hat{v}_1$.

$\#1 \sim \#9$) to one port (port $\#10$). The control to output transfer function of port $\#10$ (i.e. $\frac{\hat{v}_{10}}{\hat{\phi}_{10}}$) is simulated with and without considering losses. The conduction losses and core losses are represented by the $R_1 \sim R_{10}$, and R_m respectively.

Fig. 9 compares the calculated bode plot and simulated bode plot of the phase to voltage transfer function of the example MAB-DPP converter, with and without considering the losses. The calculate bode plot matches well with the simulated bode plot in both cases. The power conversion loss reduces the dc gain and changes the phases of the transfer function. The improved small signal model precisely capture the impact of the losses. The dominant pole $(1/\sum R_{load.i}C_i)$ of the transfer function is pushed to higher frequency by the output resistance.

B. 100-Port Very Large Scale MAB-DPP System

The small signal modeling approach described in this paper can be easily extended to model a MAB architecture with arbitrary number of ports. To validate the scalability and applicability of the approach, a 100-port SPICE simulation platform is built and tested in PLECS to capture the transfer function from $\hat{\phi}_i$ to $\hat{v}_j$ (Fig. 8) in the 100 ports. Compared to a conventional state-space based small signal model, the proposed modeling approach greatly reduces the computational load without sacrificing the model accuracy. Running SPICE simulations for large-scale MAB-DPP systems is computational heavy and time-consuming, while an analytical model can rapidly present the same results with very low computational requirements, opening the opportunities to design and optimize very large scale MAB-DPP systems. As shown in Fig. 10, the calculated bode plots match very well with the simulated results, validating the effectiveness and scalability of the proposed small-signal modeling approach.

V. Distributed Phase Shift Control Strategy

One way to control the sophisticated power flow in the MAB-DPP architecture is to decouple the control loops with an inverse matrix [6], [12], [13] and modulate the port phases with a central controller. However, these methods either have strict limitations on phase-shift or are computational heavy, making it impractical to implement them in very-large-scale MAB-DPP systems with very high number of ports. Fig. 11a illustrates the principles of a simple but robust distributed control strategy which is scalable to very large-scale MAB-DPP. Each port utilizes a feedback loop to adjust its own phase based on locally measured port voltage. As shown in Fig. 11b, the interaction between each port can be treated

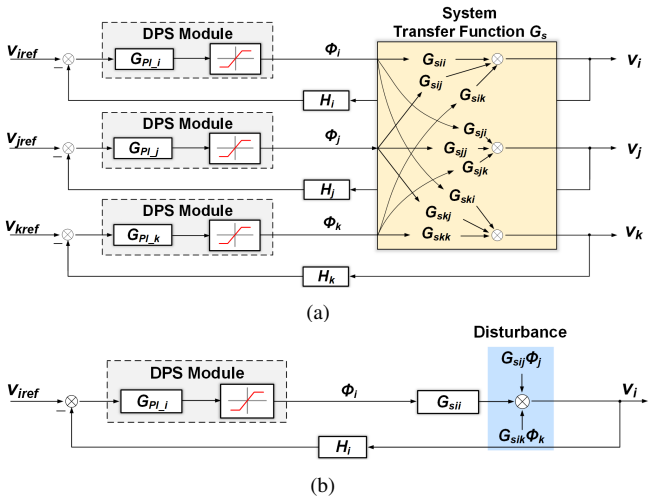

Fig. 11. (a) Principles of the modular distributed control strategy of an example 3-port MAB-DPP converter. (b) Equivalent single loop for each port.

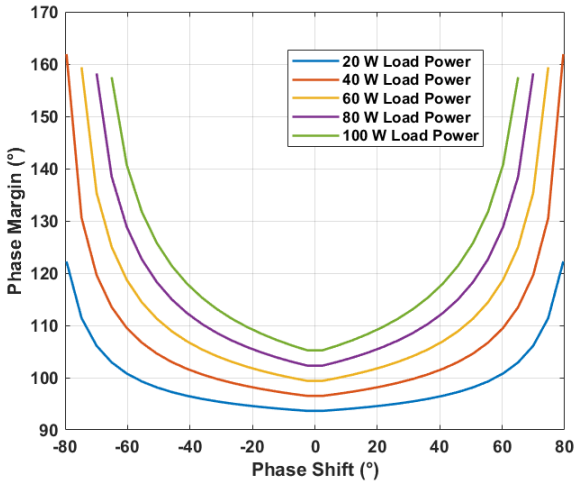

Fig. 12. Phase margin of port #1 when sweeping ϕ_1 and output power. Other ports maintain 0°phase shift and 50 W.

as disturbance. The closely coupled feedback loops can be simplified as multiple standaline feedback loops with explicit transfer function $\boldsymbol{G_s(s)}$ as captured in $(\boldsymbol{I}-\boldsymbol{G_Z G_v})^{-1}\boldsymbol{G_Z G_\phi}$ (Eq. (11)). The PI loop and phase controller of each port can be implemented as a distributed phase-shift (DPS) module that is synchronized by a system clock (Fig. 2). The DPS module can be further integrated into each half bridge to enable a fully integrated modular building block. This distributed control strategy allows independent voltage regulation of each port and can be easily applied to large-scale MAB-DPP systems with very large number of ports.

The small signal model can provide useful guidance to designing the control loops for the MAB-DPP architecture. Fig. 13a shows the calculated phase margin of $\boldsymbol{G_s(s)}$ of the 10-port MAB-DPP simulation platform with resistive load. This result indicates that the port with the lightest load and the smallest phase shift has the lowest phase margin. A PI

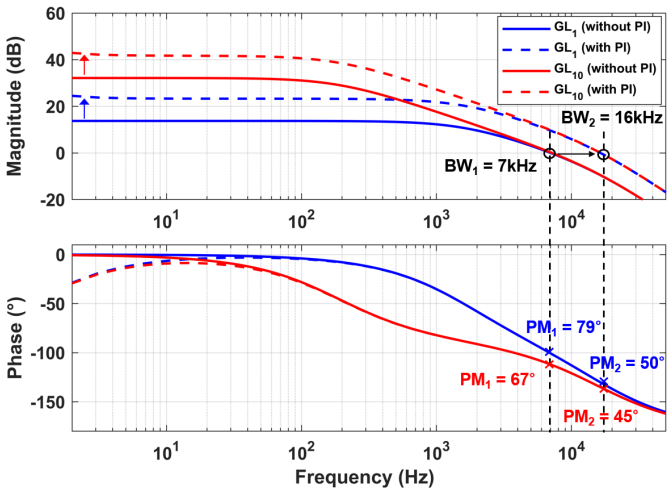

Fig. 13. Loop gain bode plot of port #1, port #10 with and without PI controller. Port #1 has the heaviest load with the largest phase margin, while port #10 has the lightest load with the lowest phase margin.

controller can be designed to eliminate the steady state error and balance the the bandwidth and phase margin of the system.

Fig. 13b shows a design example of the PI parameters in a 10-port MAB-DPP converter with distributed phase-shift control. Here, the feedback gain is considered as a delay unit, and it's delay time is one switching cycle (T). The loop gain of each port before adding a PI controller is:

$$G_{Li}(s) = G_s(s)(i,i) \times e^{-Ts} \approx G_s(s)(i,i) \times \frac{1}{1+sT}. \quad (14)$$

Fig. 13b shows the bode plots of two ports with the highest phase margin and smallest phase margin, respectively. The phase margin of both loop gains without PI are higher than $45°$. Therefore, the system bandwidth can be improved by trading off phase margin for bandwidth with a PI controller. By tuning the lowest phase margin of port $\#10$ close to $45°$, the bandwidth of all the ports was expanded. Since the lowest phase margin of 10 ports is still higher than $45°$, the distributed control loop of each port is stable. It is worth noting that, the power conversion losses of the MAB system usually shifts the phase response rightwards and increases the system phase margin, so in practice, the power losses will create additional stability margin for the system dynamic response. The system may become unstable if the phase difference between two ports is greater than $90°$. As a result, a phase limiting stage ($-45° < \phi_i < 45°$) should be included in the control loop.

VI. Experimental Verification

Fig. 14 shows the picture of a 10-port MAB-DPP converter which can support ten series-stacked 5 V voltage domains connected to a 50 V dc bus. The MAB-DPP prototype is able to process over 30 W differential power for each port. It can support a MAB-DPP system with over 300 W power rating and maintain normal operating of all the other ports while hot-swapping one port. The MAB-DPP prototype offers high efficiency and high power density. The 10-port MAB-DPP converter is 3.7 cm in radius and 1.2 cm in height with

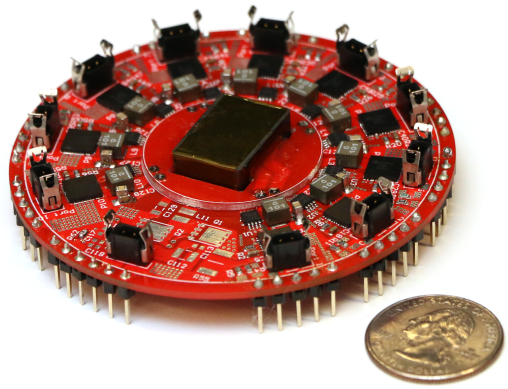

Fig. 14. A 300 W 10-port MAB-DPP converter and a U.S. quarter.

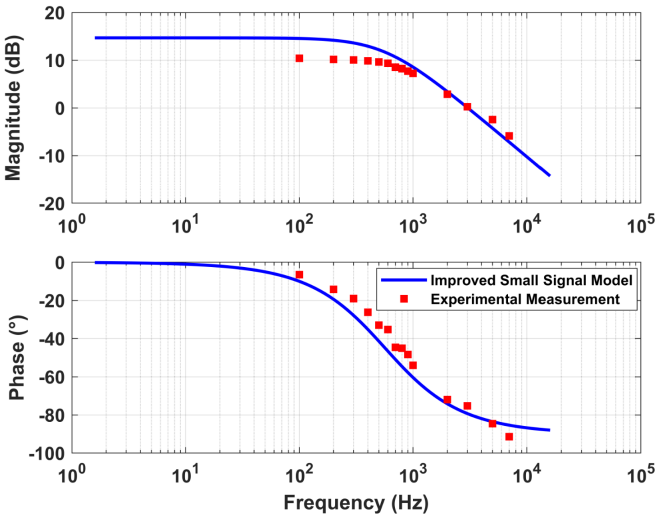

Fig. 15. Transfer function from $\hat{\phi}_{10}$ to $\hat{v}_{10}$. Switching frequency: 100 kHz. Load resistance: $R_1 \sim R_9$ is 220 Ω; R_{10} is 1.7 Ω.

a power density of over 100 W/in^3. Table II lists the detailed component parameters of the prototype (the converter topology is shown in Fig. 2).

The control to output transfer function of the 10-port prototype was measured to validate the effectiveness of the proposed small signal modeling approach. After applying a sinusoidal phase perturbation to one port, we measure the magnitude and phase response of the output voltage perturbation on the same port. Fig. 18 shows the measured voltage perturbation of port #10 with phase perturbation at three different frequencies. The reference PWM represents the zero phase-shift, and the phase perturbation is output from the DAC channel of the digital controller. Fig. 15 compares the calculated bode plot of the calculated and the measured transfer function from ϕ_{10} to v_{10} at one example operation point. The calculated and simulated bode plots show good match. The discrepancies mainly comes from the errors in the estimated resistance ($R_1 \sim R_{10}$) and magnetizing resistance (R_m), non-linear component value variations in inductors and capacitors, and other factors that the improved small signal model doesn't capture, including deadtime and switching loss.

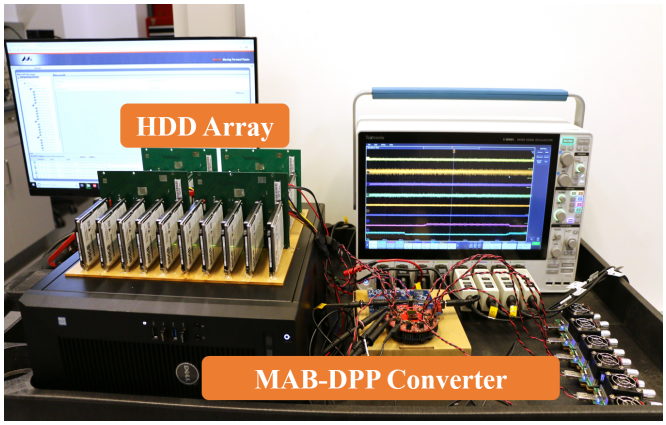

Fig. 16. Testbench of HDD server with MAB-DPP converter.

TABLE II
COMPONENT VALUES OF THE PROTOTYPE

Device Symbol	Component Description
$S_1 \sim S_{10}$	DrMOS, FDMF6833C
$C_1 \sim C_{10}$	KEMET X5R, 47 μF × 5
$C_{B1} \sim C_{B10}$	Murata X5R, 100 μF × 3
$L_1 \sim L_{10}$	Coilcraft XEL4030, 200 nH
Multiwinding Transformer	TDK EQ20, Core Material N97

Fig. 16 shows the testbench of a 10-port MAB-DPP converter suppling power to 2.5 inch HDD array connected in series. The MAB-DPP converter can support full reading, writing and hot-swapping capability of the 2.5 inch HDDs. We define the *system efficiency* of a MAB-DPP system as the total power consumed by the load (e.g., HDDs), over the total power sourced from the dc bus. The peak efficiency of the system is 99.7%. The system efficiency remains above 99% in a majority of the tested cases. We applied the distributed control strategy to the 10-port MAB-DPP converter and designed the PI parameters based on the calculated transfer function. The port voltage can maintain stable when "hot-swapping" an entire voltage domain. Fig. 17 shows the transient waveforms with an example "hot-swap" operation with a 2 A step load change. The settling time is 200 μs and the overshoot voltage is within 200 mV. It meets the transient voltage requirement of a majority of main-stream commercial 2.5 inch HDDs.

VII. CONCLUSION

This paper developed a systematic small signal modeling approach for very-large-scale MAB-DPP converter. The small signal model captures the impact of the lossy component in a MAB converter with an output resistance and can be easily extended to capture the transfer function of a MAB converter with arbitrary number of ports. The effectiveness of the small signal model is verified by SPICE simulations and experimental results. The impact of load power and phase shift on the system stability is investigated, and guidelines for designing and optimizing the control loops are provided. This paper also developed a distributed phase-shift control strategy

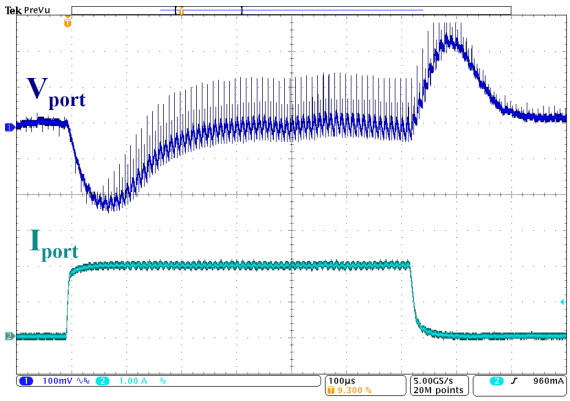

Fig. 17. Transient response of the port voltage to a 2 A load step change.

which is simple, robust and scalable. A 10-port MAB-DPP converter of 300 W power rating was designed and applied to a HDD storage server. It can maintain over 99% efficiency in majority of operating points. The proposed distributed control strategy can effectively keep voltage stable while "hot-swapping" HDDs of an entire voltage domain.

ACKNOWLEDGMENT

The authors would like to thank the DOE ARPA-E CIRCUIT program and the National Science Foundation (# 1847365) for supporting this work.

REFERENCES

[1] P. S. Shenoy, K. A. Kim, B. B. Johnson and P. T. Krein, "Differential Power Processing for Increased Energy Production and Reliability of Photovoltaic Systems," *IEEE Transactions on Power Electronics*, vol. 28, no. 6, pp. 2968-2979, June 2013.

[2] E. Candan, P. S. Shenoy and R. C. N. Pilawa-Podgurski, "A Series-Stacked Power Delivery Architecture with Isolated Differential Power Conversion for Data Centers," *IEEE Transactions on Power Electronics*, vol. 31, no. 5, pp. 3690-3703, May 2016.

[3] M. Evzelman, M. M. Ur Rehman, K. Hathaway, R. Zane, D. Costinett and D. Maksimovic, "Active Balancing System for Electric Vehicles With Incorporated Low-Voltage Bus," *IEEE Transactions on Power Electronics*, vol. 31, no. 11, pp. 7887-7895, Nov. 2016.

[4] P. Wang and M. Chen, "Towards Power FPGA: Architecture, Modeling and Control of Multiport Power Converters," *IEEE Workshop on Control and Modeling for Power Electronics (COMPEL)*, Padua, 2018, pp. 1-8.

[5] S. Falcones, R. Ayyanar, and X. Mao, "A DC-DC Multiport-Converter Based Solid-State Transformer Integrating Distributed Generation and Storage," *IEEE Transactions on Power Electronics*, 2013. 28(5): p. 2192-2203.

[6] P. Zumel, C. Fernandez, A. Lazaro, M. Sanz and A. Barrado, "Overall analysis of a modular multi active bridge converter," *IEEE Workshop on Control and Modeling for Power Electronics (COMPEL)*, Santander, 2014, pp. 1-9.

[7] H. Qin and J. W. Kimball, "Generalized Average Modeling of Dual Active Bridge DC-DC Converter," in IEEE Transactions on Power Electronics, vol. 27, no. 4, pp. 2078-2084, April 2012.

[8] K. Zhang, Z. Shan and J. Jatskevich, "Large- and Small-Signal Average-Value Modeling of Dual-Active-Bridge DC-DC Converter Considering Power Losses," *IEEE Transactions on Power Electronics*, vol. 32, no. 3, pp. 1964-1974, March 2017.

[9] F. Krismer and J. W. Kolar, "Accurate Small-Signal Model for the Digital Control of an Automotive Bidirectional Dual Active Bridge," *IEEE Transactions on Power Electronics*, vol. 24, no. 12, pp. 2756-2768, Dec. 2009.

[10] R. W. A. A. De Doncker, D. M. Divan and M. H. Kheraluwala, "A Three-Phase Soft-Switched High-Power-Density DC/DC Converter for High-Power Applications," *IEEE Transactions on Industry Applications*, vol. 27, no. 1, pp. 63-73, Jan.-Feb. 1991.

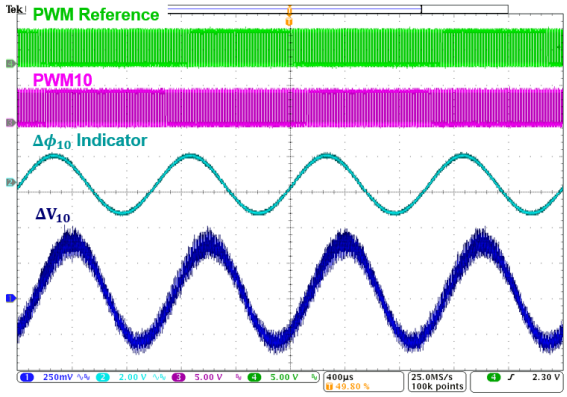

(a)

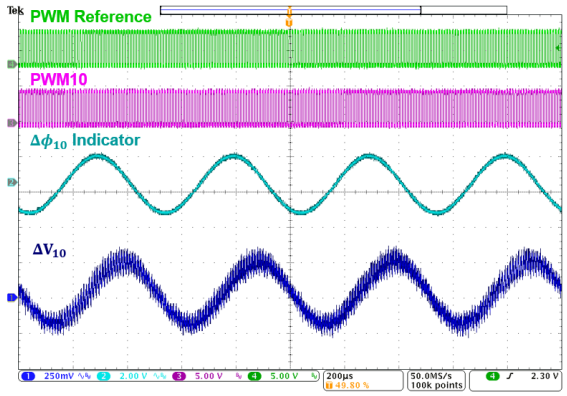

(b)

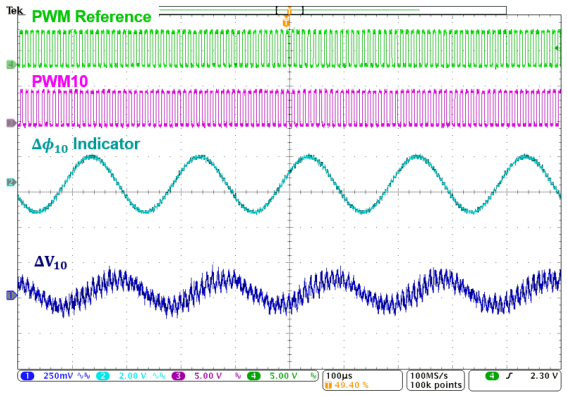

(c)

Fig. 18. Measured voltage perturbation at port #10 ($\hat{v}_{10}$) with a phase perturbation $\hat{\phi}_{10}$ at different frequencies: (a) $f = 1\ kHz$; (b) $f = 2\ kHz$; (c) $f = 5\ kHz$. Switching frequency: $100\ kHz$. Load resistance: $R_1 \sim R_9 = 220\ \Omega$; $R_{10} = 1.7\ \Omega$. Phase shift: $\Phi_1 \sim \Phi_9 = 0\ °$; $\Phi_{10} = 30.96\ °$.

[11] Y. Chen, P. Wang, H. Li and M. Chen, "Power Flow Control in Multi-Active-Bridge Converters: Theories and Applications," 2019 IEEE Applied Power Electronics Conference and Exposition (APEC), Anaheim, CA, USA, 2019, pp. 1500-1507.

[12] G. Buticchi, L. F. Costa, D. Barater, M. Liserre and E. D. Amarillo, "A Quadruple Active Bridge Converter for the Storage Integration on the More Electric Aircraft," *IEEE Transactions on Power Electronics*, vol. 33, no. 9, pp. 8174-8186, Sept. 2018.

[13] C. Zhao, S. D. Round and J. W. Kolar, "An Isolated Three-Port Bidirectional DC-DC Converter With Decoupled Power Flow Management," *IEEE Transactions on Power Electronics*, vol. 23, no. 5, pp. 2443-2453, Sept. 2008.